Three-dimensional joint inversion for magnetotelluric resistivity and static shift distributions in complex media

Yutaka Sasaki[1] and Max A. Meju[2]

[1] Accurate interpretation of magnetotelluric (MT) data in the presence of static shift arising from near-surface inhomogeneities is an unresolved problem in three-dimensional (3-D) inversion. While it is well known in 1-D and 2-D studies that static shift can lead to erroneous interpretation, how static shift can influence the result of 3-D inversion is not fully understood and is relevant to improved subsurface analysis. Using the synthetic data generated from 3-D models with randomly distributed heterogeneous overburden and elongate homogeneous overburden that are consistent with geological observations, this paper examines the effects of near-surface inhomogeneity on the accuracy of 3-D inversion models. It is found that small-scale and shallow depth structures are severely distorted while the large-scale structure is marginally distorted in 3-D inversion not accounting for static shift; thus the erroneous near-surface structure does degrade the reconstruction of smaller-scale structure at any depth. However, 3-D joint inversion for resistivity and static shift significantly reduces the artifacts caused by static shifts and improves the overall resolution, irrespective of whether a zero-sum or Gaussian distribution of static shifts is assumed. The 3-D joint inversion approach works equally well for situations where the shallow bodies are of small size or long enough to allow some induction such that the effects of near-surface inhomogeneity are manifested as a frequency-dependent shift rather than a constant shift.

1. Introduction

[2] Advances in three-dimensional (3-D) magnetotelluric (MT) inversion [e.g., *Mackie and Madden*, 1993; *Newman and Alumbaugh*, 2000; *Sasaki*, 2004; *Siripunvaraporn et al.*, 2005] have brought the method within range of its theoretical resolving power, but static shift remains the bane of practical MT exploration [*Meju*, 2002] and yet little attention has been devoted to appropriately accounting for this effect in 3-D inversion so as to obtain an accurate interpretation of field data. The static shift effect is due to the ubiquitous presence of small-scale near-surface inhomogeneities and manifests as a vertical shift of the apparent resistivity curve by a constant multiplicative factor, without any corresponding change in the phase curve [e.g., *Berdichevsky and Dmitriev*, 1976]. This effect varies from site to site and differs for different measurement directions. In the more common 2-D linear surveys, partial remedies to this problem are provided by interpretation based on known geology [e.g., *Jones*, 1988], tensor decomposition method [e.g., *Groom and Bailey*, 1989], correction for static shifts using collocated transient electromagnetic (TEM) measurements [e.g., *Sternberg et al.*, 1988; *Pellerin and Hohmann*, 1990; *Meju*, 1996, 2005], and spatial filtering of continuously sampled electric fields [*Torres-Verdin and Bostick*, 1992]. In the typical MT surveys where additional TEM or continuous electric field measurements are not made, joint inversion for static shift and resistivity is considered the best approach for tackling the static shift problem in two dimensions [*deGroot-Hedlin*, 1991; *Ogawa and Uchida*, 1996]. This concept was extended recently into three dimensions [*Sasaki*, 2004]. However, there are limitations in the way that the numerical experiments mimicking the field occurrence of static shift were simulated in these multidimensional inversion studies. For example, in the 3-D approach of *Sasaki* [2004], the actual apparent resistivities computed for a large-scale conductivity structure with an embedded 3-D body were "static shifted" using random values from a Gaussian distribution with a zero mean and an assumed standard deviation. This means that they do not reflect an important phenomenon of static shift, which is that it arises below some particular value of frequency rather than as a constant shift throughout the whole measured frequency range. Also, the different geometrical forms of surficial overburden that commonly distort MT soundings were not considered.

[3] In an effort to test 3-D inversion algorithms in realistic situations, we take the approach of generating more realistic static-shifted data by virtue of the model geometry

[1]Department of Earth Resources Engineering, Kyushu University, Fukuoka, Japan.
[2]Department of Environmental Science, Lancaster University, Lancaster, UK.

itself. An important thrust of this paper is to clarify whether it is simply enough to invert regional grid-like MT surveys in three dimensions without paying adequate attention to the problem of static shift, and to determine whether static shift can be accurately predicted in complex media with 3-D overburden such as typify many regions of the world. We therefore use the knowledge gained from examining some well-controlled MT measurements in different geological environments to construct a realistic model for simulating static effects in 3-D media, invert the data without any correction for these near-surface influences and then compare the performance of our 3-D regularized inversion methods that employ different statistical constraints on the distribution of static shift. Since the ubiquitous presence of a heterogeneous overburden in most geological terrains causes undesirable geological noise in MT measurements, it is instructive to first, place the static shift problem in the proper geological context so as to determine the relevant constraints on the inverse problem of joint resistivity and static shift estimation.

1.1. Geological Constraints: Forms of Overburden and Patterns of Static Shift

[4] The geological processes of weathering, erosion and deposition influence the nature of the overburden to a large extent and are thus the critical factors to consider in any analysis of MT static shift. For convenience, we distinguish two types of overburden, namely, (1) residual and unconformity-related deposits formed in situ which includes products of weathering, karstification, and exhalative hydrothermal alteration, and (2) transported overburden which includes granular deposits laid down by wind, water and volcanic eruptions. Both forms of overburden may be laterally discontinuous (forming randomly distributed surficial patches) or very extensive (forming blanket-type cover deposits or elongate trends such as channel fill or wadi-type deposits common in past-glaciated terrains and highly weathered mineralized bodies (gossans) found in some Precambrian shield areas [Meju, 2002]). Weathering of crystalline rocks is common in tropical and subtropical environments, but preserved weathered layers may be found in areas not presently favorable to the process of deep weathering [Palacky, 1987]. The weathered layer is of variable thickness and may contain a water-saturated chloritization zone (or saprolite) and an upper unsaturated zone, depending on the type of lithology [Palacky, 1987; Meju et al., 2001]. The saprolite zone has been identified in many regions of the world as the most electrically conductive layer in a weathered section while the capping oxidized zone (duricrust) is usually relatively hardened and electrically resistive [Palacky, 1987; Meju, 2002]. The occurrence of surficial resistive and conductive patches or elongate gossanous bodies in a weathered crystalline terrain has implications for static shift in MT surveying. Clastic cover deposits originating from the erosion of preexisting rocks or pyroclastics can also exhibit heterogeneities, depending on their mode of transport and deposition, grain size distribution, and porosity. For example, well-sorted clastic sediments may be somewhat homogeneous at the scale of MT measurements (the alluvial fill deposits in the Basin and Range graben are commonly represented by a homogeneous patch with large lateral dimensions [Wannamaker et al.,

1984]), while volcanogenic deposits are heterogeneous with pillow and slump features common in marine deposits. Glacial and interglacial (e.g., solifluxion and lacustrine) deposits may comprise sands and gravels (torrent and outwash deposits and those within boulder clay and stream sediments or wadis). Such deposits may be characterised by an upper unsaturated zone and a basal water-saturated zone depending on their hydraulic properties and climatic conditions. They are typically associated with lateral changes in resistivity in the near-surface and hence static distortions of apparent resistivity sounding curves [cf. Meju, 2005].

[5] We have reanalyzed some available field data comprising high-quality collocated tensor MT and multigeometry TEM soundings along individual survey lines in different geological settings [Meju, 1996; Danladi, 1997; Simpson et al., 1997; Meju et al., 1999; Mohamed et al., 2002; Sakkas et al., 2002] to gain some practical insight into possible geological and statistical constraints on static shifts and hence place the inverse problem within a robust geological framework. We sought to understand the pattern of variation of overburden resistivity and static shift with lithology at different spatial scales using soundings for which the station intervals ranged from 1 km (in a small-scale survey) to 20 km (in a large-scale regional survey). Thus, for a given sounding site, we determined the anomalous overburden resistivity (AOR) by inverting central loop TEM data, we computed the static shift parameters in the log domain (s) for the dual-mode MT apparent resistivity curves using collocated multigeometry (central, single, and offset loop) TEM soundings, and these parameters (AOR and s) were then evaluated against the local geology for any significant patterns for each survey line. The detailed results are given in Tables A1 to A4 in Appendix A.

[6] There are significant variations in overburden resistivity and static shift for all the survey lines attesting to the ubiquity of the static shift problem. The mean static shift is -0.05 for a regional transect with 1 km station spacing in Cyprus, -0.10 and -0.25 for two regional transects with $10-20$ km station spacing in Parnaiba basin in Brazil and 0.10 over a regional transect with $10-20$ km station spacing in southern Kenya. Analysis of the static shift patterns in the light of geological data (Tables A1 to A4) appears to suggest some correlation between geological environment and the amount and sense of static shift. There is a net downward shift in MT sounding curves in deeply weathered regions or sedimentary terrains with conductive overburden including submarine volcanics as in Cyprus and Parnaiba basin (Tables A1 to A3). There is a net upward shift in regions of recent volcanic activities such as southern Kenya where the weathered layer may not be well developed and the magnitude of static shift for individual sites could be large (Table A4). The frequency distributions of static shift in the various geological terrains are shown in Figure 1. There appears to be good support for a Gaussian distribution of static shift, but it is skewed depending on the given geological environment.

1.2. Static Shift Model for 3-D Surveying in Complex Media

[7] To evaluate the effects of static shift on 3-D surveys and the capability of 3-D inversion methods for accurately
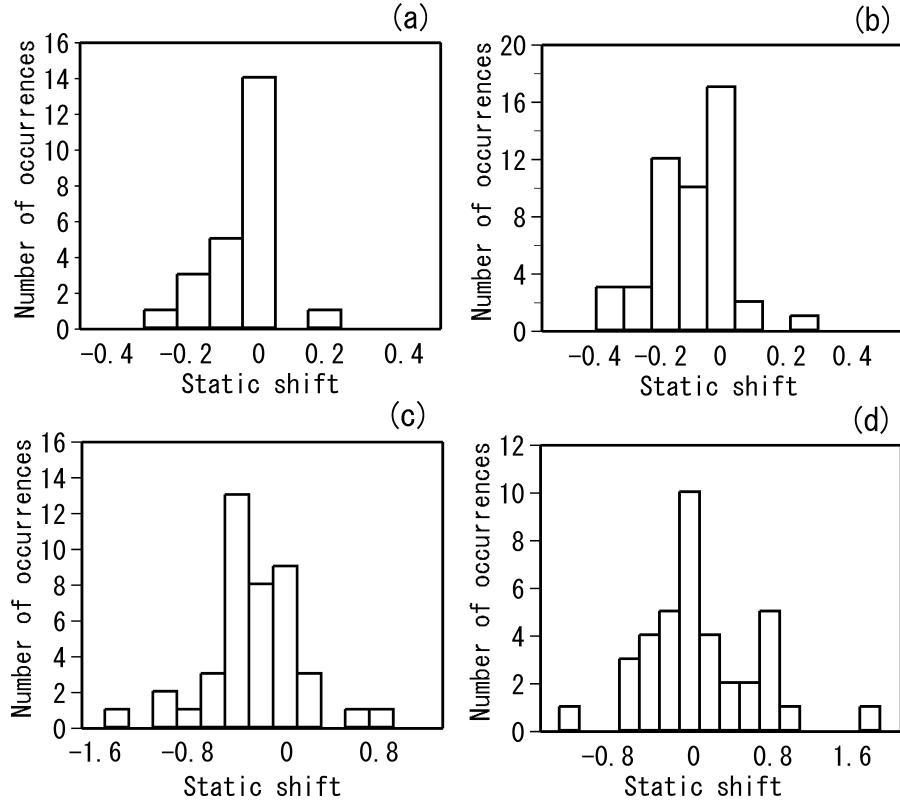
Figure 1. Histograms of dual-mode static shifts in MT surveys with different spatial sampling in various geological environments. The frequency distributions are for (a) 1 km sampling over a spreading ridge structure in northeast Troodos, Cyprus; (b) and (c) 10–20 km and 10 km sampling in eastern and southern sectors of Parnaiba basin in Brazil, respectively; (d) 10–20 km sampling across the Kenya rift. The static shifts are shown in the log (base 10) domain. Details of the original data and static shift parameters are given in Tables A1 to A4 in Appendix A.

predicting static shifts in realistic geological situations, we have selected a synthetic model of a complex medium shown in Figure 2 over which we superimpose a blanket-like or elongate overburden as suggested by the geological considerations presented above. The test model consists of four layers with inhomogeneities embedded in the upper three layers. The first layer includes a $3.5 \times 3.5 \times 0.9 \text{ km}^3$ body with a resistivity of 500 ohm m in the central part of the plan view, in addition to the two different forms of surface overburdens described below. The second layer includes a horizontal square slab having dimensions $5 \times 5 \times 0.5 \text{ km}^3$ and a resistivity of 30 ohm m. In the third layer, a vertical contact separates media of resistivities 2000 and 200 ohm m. To simulate static shifts that are consistent with geological observations, we consider two extreme cases for the overburden, namely, (1) heterogeneous discontinuous patches and (2) elongate homogeneous bodies (i.e., long enough to allow some induction as well as current channeling). The thickness for both forms of overburden is fixed at 100 m. For the first case, we divide a $12 \times 12 \text{ km}^2$ area of overburden (labeled A in Figure 2) into 576 contiguous blocks of the same dimensions ($500 \times 500 \times 100 \text{ m}^3$) and assigned Gaussian random numbers for the resistivity of blocks. We assume that the resistivities of the overburden blocks have a Gaussian distribution with a mean of 300 ohm m and a standard deviation of 0.3 in the log

scale. Note that this is philosophically different from *Sasaki* [2004] where the apparent resistivities were static shifted using random values from a Gaussian distribution with a zero mean. For the second case, we consider an $11 \times 3 \text{ km}^2$ area of elongate homogeneous overburden (labeled B in Figure 2) of 200 ohm m.

[8] 36 MT soundings at 15 frequencies from 0.1 to 320 Hz were simulated using a staggered grid finite difference method. The observation sites are uniformly spaced at 2 km intervals in both the *x* and *y* directions. The finite difference method used here is similar to that of *Sasaki* [2004] incorporating *Smith*'s [1996] correction procedure that enforces divergence-free conditions on the current density in the Earth and the electric field in the air, but solves for the secondary electric fields to ensure the accuracy for large-scale forward problems. The model including the air region was discretized into a $68 \times 68 \times 38$ cell grid with the smallest cell size of $250 \times 250 \times 40 \text{ m}^3$ in the near surface below the sites.

[9] Figure 3 shows the responses of the model with a heterogeneous overburden (model A) calculated for the *xy* and *yx* directions at two selected sites (23 and 34 in Figure 2), together with the corresponding responses for the case where the overburden has a uniform resistivity of 300 ohm m. The apparent resistivity curves for soundings over the heterogeneous overburden (circles) are shifted
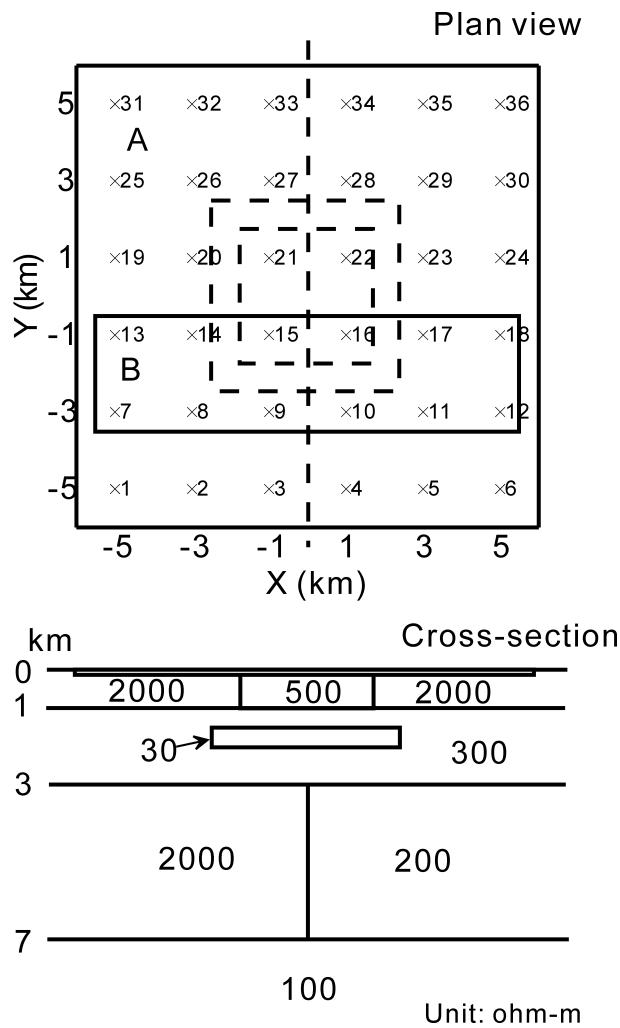
Figure 2. The 3-D model used to generate synthetic MT data. The model has a surface overburden labeled either A or B. Crosses in the plan view show MT site locations.

relative to those over the homogeneous overburden (solid lines) for the whole frequency range, while the corresponding phase curves are almost identical. Figure 4 shows the histogram of static shifts produced for all the sites. It can be seen that the distribution of static shift is roughly Gaussian but has a somewhat longer tail downward. Figure 5 shows the responses of the model with a homogeneous elongate overburden (model B) at two selected sites (13 and 14 in Figure 2), together with the corresponding responses for the case where the overburden is not present. The departures from parallel shifts in the apparent resistivity curves are seen at high frequencies while the departures of the phase curves from the undistorted ones are more obvious above some lower threshold frequency. This feature of the MT responses suggests that in the overburden (frequency-dependent) induction effect becomes important rather than current channeling at high frequencies. Thus, strictly speaking, such distortions cannot be regarded as "static" shifts for the frequency range considered. Resistivity structure in nature is considered to include near-surface inhomogeneities of various forms and spatial scales, so it is likely that both types of distortion

(complete and partial shifts) are present in any given survey area. The relevant hypothesis to test here is whether the assumption of a Gaussian static shift is a necessary constraint for effective simultaneous 3-D estimation of both resistivity and static shift parameters in complex media with near-surface inhomogeneities.

2. Methodology for 3-D Joint Resistivity and Static Shift Estimation

[10] Static shift of MT data is manifested as a vertical displacement of the apparent resistivity curve when plotted on a log-coordinate scale. Thus the relationship between the observed data composed of log apparent resistivities and phases, $\mathbf{d}_o$, the theoretical responses that are not affected by static shift, $\mathbf{d}$, and the additive static shift parameters $\mathbf{s}$ may be written as

$$\mathbf{d}_o = \mathbf{d} + \mathbf{G}\mathbf{s}, \tag{1}$$

where $\mathbf{G}$ is a matrix relating static shift values to the data. Note that rows of $\mathbf{G}$ corresponding to phases are zeros, because they are not affected by static shift. *deGroot-Hedlin* [1991] posed the inverse problem as finding both the static shift parameters and the smoothest resistivity distributions that fit the MT data under the constraint that the sum of
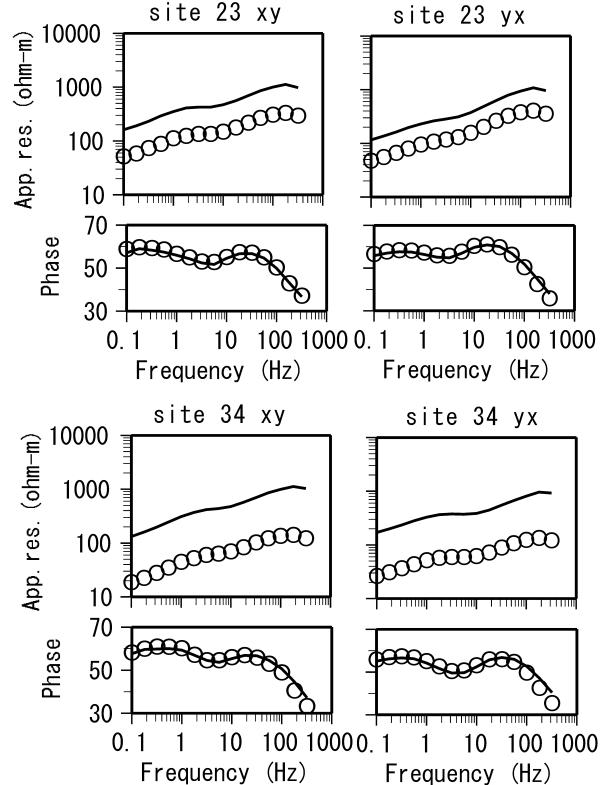

Figure 3. Apparent resistivity and phase curves for the *xy* and *yx* directions at sites 23 and 34 for the model with a heterogeneous overburden (model A). The solid lines represent the responses for the model having the uniform overburden, while open circles are for the model with the heterogeneous overburden.
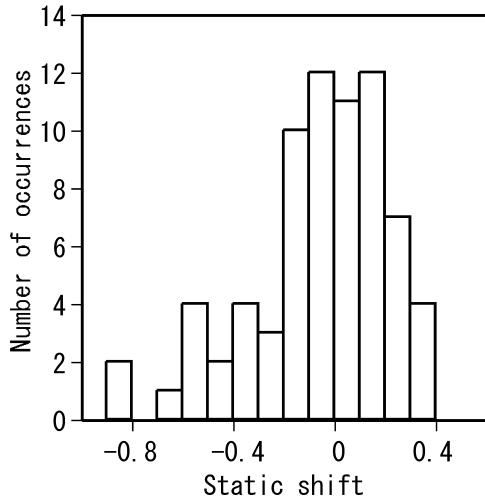
Figure 4. Histogram of the static shifts in 72 apparent resistivity curves derived for the test model.

static shifts equates to zero. This is equivalent to finding a solution that minimizes the function

$$U = Q + \alpha^2 R + \beta^2 S, \qquad (2)$$

where α and β are Lagrange multipliers, Q is a measure of the data misfit, R is the roughness measure operating on the model, and $S = \left[\sum_i S_i \right]^2$ is added to impose a constraint on static shift parameters. The misfit measure may be written as

$$Q = \parallel \mathbf{W}[\mathbf{d}_o - \mathbf{F}(\mathbf{m}) - \mathbf{Gs}] \parallel^2, \qquad (3)$$

where $\mathbf{W}$ is a diagonal matrix whose elements are the reciprocal of the measurement uncertainties, and $\mathbf{F}(\mathbf{m})$ denotes the forward modeling functional that predicts the data for a given model $\mathbf{m}$. The roughness measure is defined by

$$R = \parallel \mathbf{Cm} \parallel^2, \qquad (4)$$

where $\mathbf{C}$ is a second-difference (Laplacian) operator used to quantify the model roughness.

[11] Because the forward functional is nonlinear, an iterative scheme is used which is based on linearizing equation (3) about an initial model $\mathbf{m}^{(0)}$. If $\Delta \mathbf{m}$ is the perturbation from the initial model, then equation (3) is linearized as

$$Q \approx \parallel \mathbf{W}[\Delta \mathbf{d} - \mathbf{A}\Delta \mathbf{m} - \mathbf{Gs}] \parallel^2, \qquad (5)$$

where $\mathbf{A}$ is the sensitivity matrix, or the matrix of first-order derivative of $F(\mathbf{m})$ with respect to $\mathbf{m}$ and

$$\Delta \mathbf{d} = \mathbf{d}_o - \mathbf{F}\left(\mathbf{m}^{(0)}\right) \qquad (6)$$

is the discrepancy vector containing the differences between the observed and predicted data. The minimization of the

functional U is equivalent to obtaining the least squares solution of the augmented (rectangular) system

$$\begin{bmatrix} \mathbf{WA} & \mathbf{WG} \\ \alpha \mathbf{C} & \mathbf{0} \end{bmatrix} \left\{ \begin{matrix} \Delta \mathbf{m} \\ \mathbf{s} \end{matrix} \right\} = \left\{ \begin{matrix} \mathbf{W}\Delta \mathbf{d} \\ -\alpha \mathbf{Cm}^{(0)} \end{matrix} \right\}. \qquad (7)$$

The constraint on static shift is incorporated into equation (7) by appending a row of ones to the matrix $\mathbf{G}$, a row of zeros to $\mathbf{A}$, and a zero to $\Delta \mathbf{d}$, with the corresponding diagonal of $\mathbf{W}$ being β.

[12] Assuming a Gaussian distribution for static shifts, *Ogawa and Uchida* [1996] presented a variant of the above formulation in which they redefine S as $\parallel \mathbf{s} \parallel^2$. This approach yields the system

$$\begin{bmatrix} \mathbf{WA} & \mathbf{WG} \\ \alpha \mathbf{C} & \mathbf{0} \\ \mathbf{0} & \beta \mathbf{I} \end{bmatrix} \left\{ \begin{matrix} \Delta \mathbf{m} \\ \mathbf{s} \end{matrix} \right\} = \left\{ \begin{matrix} \mathbf{W}\Delta \mathbf{d} \\ -\alpha \mathbf{Cm}^{(0)} \\ \mathbf{0} \end{matrix} \right\}, \qquad (8)$$

where $\mathbf{I}$ is the identity matrix.

[13] Note that if, as an alternative hypothesis, we assume that the static shift arising from a given surficial 3-D body will vary smoothly in amplitude with distance based on the physics of the problem, we can place a weak constraint on the site-to-site variation in the amplitude of $\mathbf{s}$ in *xy* and *yx* directions by defining instead
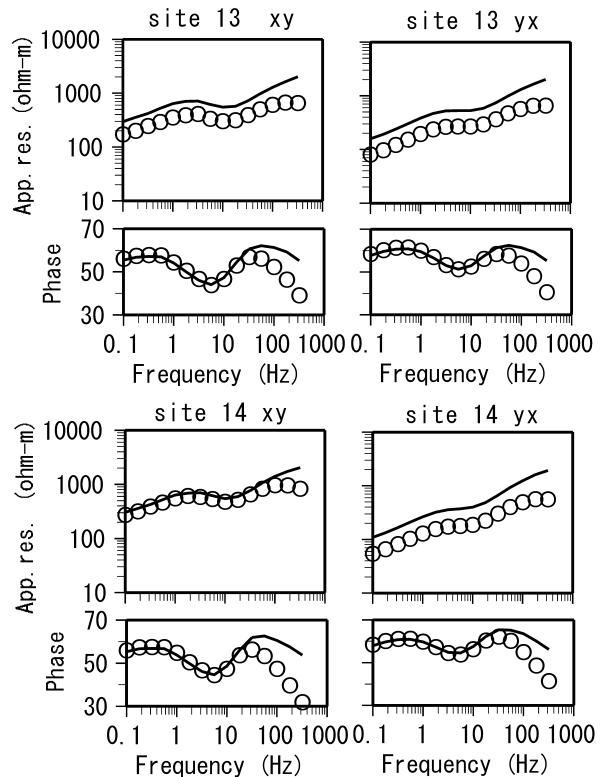

Figure 5. Apparent resistivity and phase curves for the *xy* and *yx* directions at sites 13 and 14 for the model with an elongate homogeneous overburden (model B). The solid lines represent the responses for the model having no overburden, while open circles are for the model having the elongate overburden.
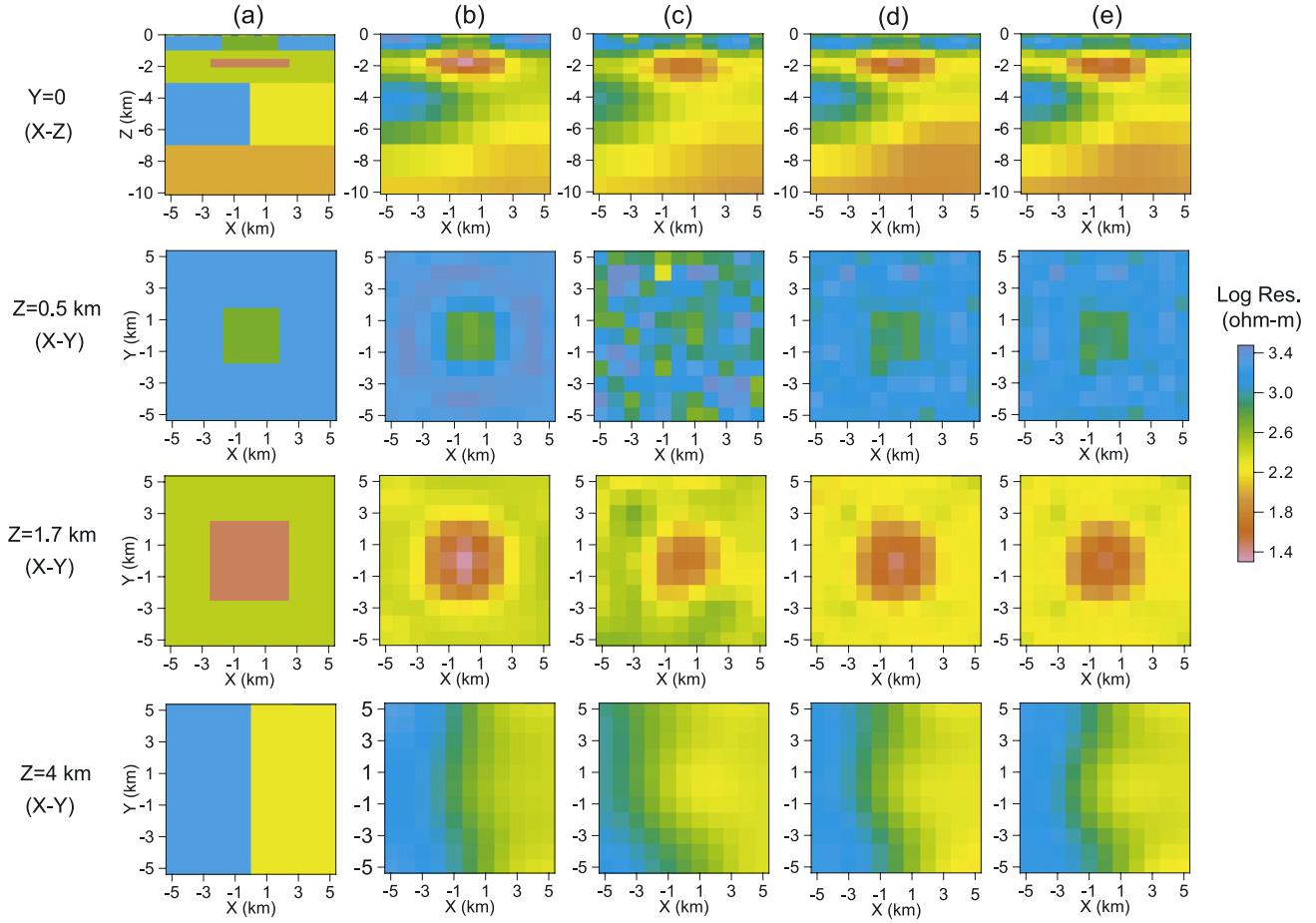
Figure 6. Resistivity distributions recovered by 3-D inversion for the model with a heterogeneous overburden (model A). (a) True model and (b) inversion result when static shifts are not present. Results obtained by inverting the same static shifted data under different conditions for (c) inversion without accounting for static shifts; (d) inversion using Gaussian constraint; and (e) inversion using zero sum constraint. The first row shows the respective vertical sections at $y = 0$. The second to fourth rows show horizontal sections at depths of 0.5, 1.7, and 4 km.

Figure 7. Convergence curves showing data misfit versus iteration number for the four inversions whose results are shown in Figures 6b, 6c, 6d, and 6e.

Figure 8. Plots of the final data misfit versus the parameter β for the simultaneous inversions using Gaussian (circles) and zero sum (triangles) constraints.

Figure 9. Comparisons of true static shifts (solid lines) and those recovered by 3-D joint inversions using Gaussian (circles) and zero sum (triangles) constraints for the model with the heterogeneous overburden. (a) The xy direction and (b) the yx direction.

$$S = \parallel \mathbf{Hs} \parallel^2, \qquad (9)$$

where H is a second-difference operator. This approach leads to the system of equations

$$\begin{bmatrix} \mathbf{WA} & \mathbf{WG} \\ \alpha\mathbf{C} & 0 \\ 0 & \beta\mathbf{H} \end{bmatrix} \begin{Bmatrix} \Delta\mathbf{m} \\ \mathbf{s} \end{Bmatrix} = \begin{Bmatrix} \mathbf{W}\Delta\mathbf{d} \\ -\alpha\mathbf{Cm}^{(0)} \\ 0 \end{Bmatrix}. \qquad (10)$$

Equations (7), (8) and (10) can be solved by the modified Gram-Schmidt method, singular value decomposition, or QR decomposition using Householder transformation. We used the modified Gram-Schmidt method in the inversion studies that we report next.

3. Three-Dimensional Inversion Studies

[14] In the numerical experiments, we assume that the data have the same standard deviations and define, as our model acceptance criterion, the RMS measure

$$Q_{rms} = \sqrt{\frac{1}{N} \sum_{i=1}^{N/2} \left\{ \left(\ln\frac{\rho_{ai}^o}{\rho_{ai}^p} \right)^2 + w^2 \left(\phi_i^o - \phi_i^p \right)^2 \right\}}, \qquad (11)$$

where ρ_{ai} is the apparent resistivity, ϕ_i is the phase in degrees, the superscripts o and p refer to observed and predicted data respectively, and N is the number of data points. The scaling factor w represents the weight assigned to the phase relative to the apparent resistivity and is set to $2\pi/180$ so as to honor the relative standard deviation. Note that this is tantamount to equating the phase error in radians

to half the relative error of apparent resistivity. The input data for the present inversion studies are the apparent resistivities and phases calculated from the off-diagonal impedance elements along the (x, y) coordinate system; note that it is desirable to invert on the rotated apparent resistivities and phases if some of the on-diagonal impedance elements are large in the original coordinate system. Prior to inversion, 1.5 percent Gaussian random noise was added to the impedance elements, which translates to standard deviation of 3 percent for the apparent resistivity and 0.86 degrees for the phase. In the inversions, a $42 \times 42 \times 34$ grid with a minimum cell size of $500 \times 500 \times 125$ m^3 was used for the forward modeling, and the Earth was divided into 1573 ($11 \times 11 \times 13$) blocks of unknown resistivity. All the inversions started from a homogeneous half-space of resistivity 200 ohm m and were terminated at the seventh iteration. Unlike *Sasaki* [2004], the full sensitivity matrix was constructed at each iteration.

3.1. Results for Model With Heterogeneous Overburden

[15] We first present inversion results for the model with the heterogeneous overburden (model A). The size of the blocks below the sites used in the inversion was $1000 \times 1000 \times 250$ m^3, which is larger than that of the overburden blocks in the actual model ($500 \times 500 \times 100$ m^3). Thus this synthetic example represents a situation in which the near-surface inhomogeneities causing static shifts are too small to be recovered from inversion. Figure 6 shows the models obtained from four different 3-D inversion studies, together with the true model. Figure 6b shows the image reconstructed from inversion for the case where no static shifts are present (i.e., where the surface overburden has a uniform resistivity 300 ohm m), which serves as a reference image in examining how the presence of static shifts influences inversion results. Figures 6c, 6d, and 6e show the models from inversions of the same data having static shifts. In Figure 6c, static shifts are not taken into account, while in Figures 6d and 6e they are estimated based on the Gaussian and zero sum assumptions, respectively. We experimented with placing smoothness constraints on the static shift parameters (equation (10)) but this did not lead to any significant improvement in static shift estimation and it would serve no further purpose to present this particular result here.

[16] The convergence information in the form of data misfit versus iteration number is shown in Figure 7 for the reconstructed 3-D images presented in Figure 6. We see from Figure 7 that in the inversion of static shift-free data, the data misfit Q_{rms} converges to a value closest to the assumed noise level (0.03). The discrepancy is probably attributed to numerical differences between cell discretization used to generate synthetic data and that used in the inversion. We also see that inverting static shifted data without taking into account their effects results in a poor convergence; the model shown in Figure 6c is the one obtained at the third iteration where the data misfit reaches the minimum value. The two static shift removal methods reduce the data misfits to almost the same final value, with very similar convergence in the later stage of the iterations.

[17] The model in Figure 6c shows that ignoring the presence of static shifts does distort the resistivity image

Figure 10. Resistivity distributions recovered by 3-D inversion for the model with an elongate homogeneous overburden (model B). (a) True model and (b) inversion result obtained without accounting for static shifts. (c) and (d) Inversion models obtained using Gaussian and zero sum constraints, respectively. The first row shows the respective vertical sections at $y = 0$. The second to fourth rows show horizontal sections at depths of 0.5, 1.7, and 4 km.
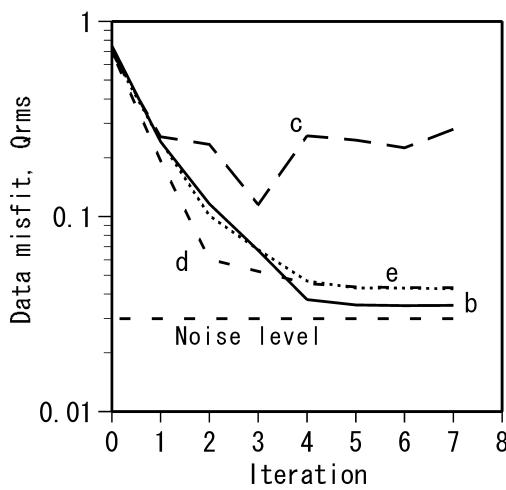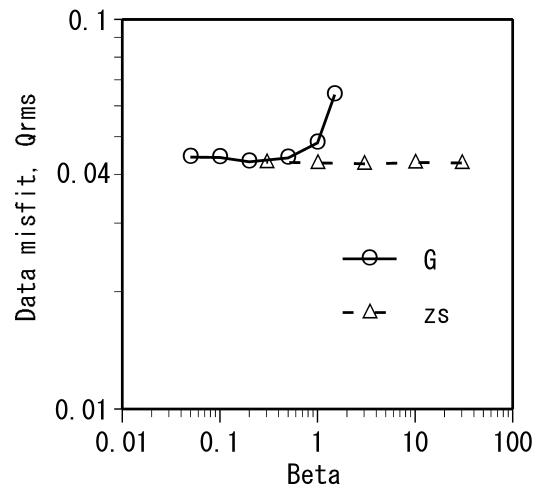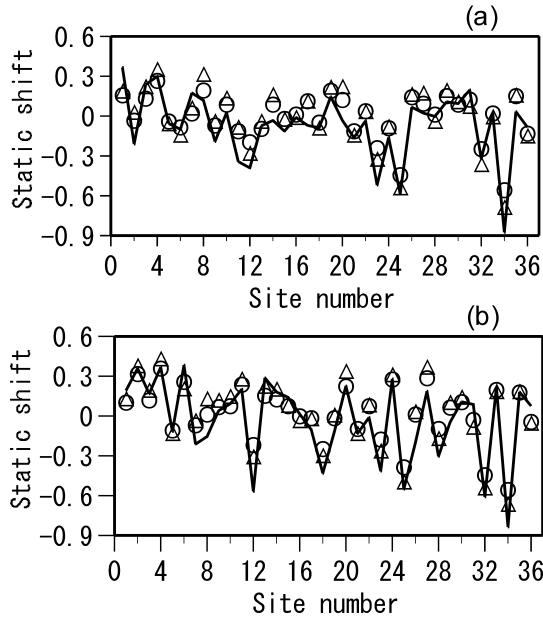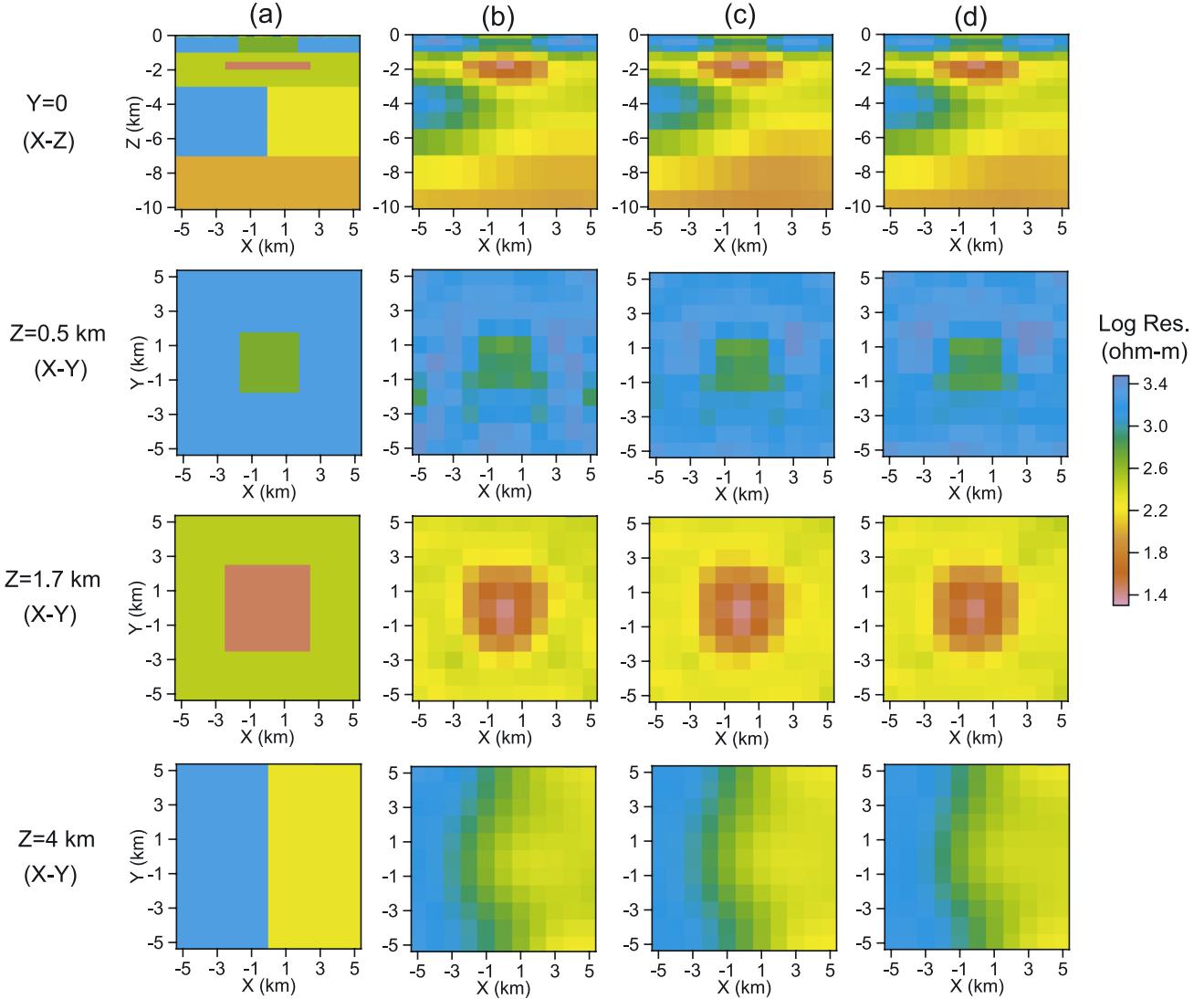
in 3-D inversion especially at shallow depth (within about 1 km for this particular example); the distortion is less severe for large-scale structure but is still significant. It is comforting to note that the large-scale feature at great depth is somewhat satisfactorily recovered by 3-D inversion in contrast to 1-D and 2-D synthetic examples [e.g., *deGroot-Hedlin*, 1991] where the models recovered from inversion are far from the true ones when static shifts are not removed. However, this may not be surprising if one notes that unlike in 1-D and 2-D TE mode inversions, static shift effect is simulated in 3-D inversion by incorporating near-surface structure where it is needed to fit the data, even though it cannot properly represent the true structure. Note that in 3-D inversion the phase is not influenced by the near-surface inhomogeneities produced as long as their dimensions are much smaller than the skin depth. The models obtained by

the static shift removal methods in Figures 6d and 6e are very similar, suggesting that there is virtually no difference in the performance between the two methods. It is also shown that the methods reduce near-surface artifacts significantly and improve the overall model resolution.

[18] The values of β chosen are 0.2 and 3.0 for the inversions assuming Gaussian and zero sum shifts, respectively, because they gave the smallest data misfit among our trial values. It is evident from Figure 8 that inversion assuming zero sum shift is insensitive to β while this is not the case for inversion assuming a Gaussian shift; however, the choice of β is not critical below some threshold value. The value of α is determined at each iteration using a line search so that the smallest misfit is achieved. This typically requires three or four trial values. In Figure 9, the recovered static shifts (symbols) are compared
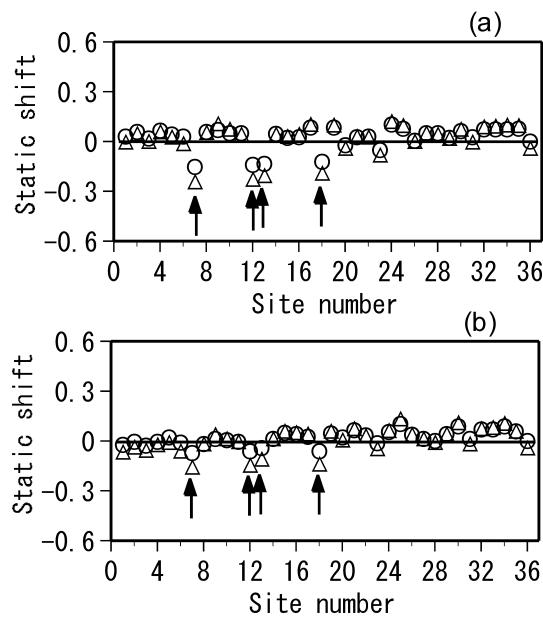
Figure 11. Static shifts recovered by the 3-D joint inversion using Gaussian (circles) and zero sum (triangles) constraints for the model with an elongate homogeneous overburden. The arrows indicate relatively large negative static shifts for the sites near the corners of the overburden. (a) The *xy* direction and (b) the *yx* direction.

with true shifts (solid lines). The comparisons are generally good. However, as also noted in the 2-D case by *Ogawa and Uchida* [1996], the absolute values of shifts tend to be larger in the case of zero sum assumption (triangles) than Gaussian assumption (circles). Nevertheless, it can be said that both procedures can recover static shifts equally well in complex 3-D media.

3.2. Results for Model With Elongate Homogenous Overburden

[19] Our next experiment employs the model with the homogeneous overburden (model B). We noted earlier that the distortions caused by this surface inhomogeneity are frequency dependent at high frequencies and thus cannot be regarded as static shifts. One question to be addressed here is whether the simultaneous inversion that assumes "static" shifts suffers any adverse effects from this type of distortion. We show in Figure 10 the models obtained by carrying out three different inversion runs. Figure 10b shows the model obtained from the inversion assuming no static shifts. Figures 10c and 10d show inversion models when assuming Gaussian and zero sum static shifts, respectively. The data misfits for the models in Figures 10b, 10c, and 10d are 0.037, 0.036, and 0.036, respectively. The values of β used in the simultaneous inversions are the same as in the previous example. It appears (Figure 10) that there is virtually no difference between the inversion results, whether static shift parameters are included or not. It is also important to note that while the thickness of the actual overburden (100 m) is much smaller than that of the uppermost inversion blocks (250 m), the presence of the overburden

does not cause any problems in inversion results except for some perturbations seen beneath the overburden (see Figure 10, second row). This indicates that the effects of such an overburden are mostly absorbed in the uppermost layers of the inversion model. This is mainly because as shown in Figure 5, the phase response due to the overburden is significant at high frequencies and is limited to high frequencies [*Wannamaker et al.*, 1984]. Figure 11 shows the static shifts estimated using Gaussian (circles) and zero sum (triangles) constraints. The estimated values are generally close to zero as expected, but four negative shifts indicated by arrows are noticeable. These shifts are obtained for sites 7, 12, 13, and 18, which are all located near the corners of the overburden, and reflect the fact that the contribution of current channeling in the overburden are relatively significant for these sites. Note that static shift can arise even for a homogeneous overburden with large lateral dimensions depending on how close the site is placed to the contact. We see from this experiment that the simultaneous inversion is still effective in recovering resistivity distribution even if the effects of near-surface structure include frequency-dependent shifts.

4. Conclusions

[20] A reappraisal of selected well-controlled MT field measurements in different environments has yielded some geological insights into the nature and distribution of static shift. On the basis of these geological observations, we have simulated representative regional 3-D surveys to show how near-surface resistivity structure influences 3-D inversion and how the joint estimation of resistivities and static shifts improves the interpretation. One interesting feature about 3-D inversion in the presence of static shifts is that in spite of poor convergence, it is capable of recovering large-scale structure relatively well compared to 1-D and 2-D cases. This is because the 3-D forward modeling used within the inversion compensates for static shifts to some extent by incorporating near-surface structure even if it is not an accurate representation of the true structure. However, it is also true that ignoring static shifts leads to distortions of smaller-scale structure and addition of artifacts produced at shallow depth in the inverted model. On the other hand, joint inversion for

Table A1. Variation of Overburden Resistivity and Static Shift Along a Regional Transect With 1 km Station Spacing in Northeast Troodos, Cyprus[a]

Station	AOR, Ω m	S-TE	S-TM	Local Geology
Sha1	223	0	0.223	basal group
Sha3	150	−0.114	−0.174	sheeted dykes
Sha5	14	−0.097	−0.204	pillow lavas
Sha6	6	0	−0.114	pillow lavas
Sha7	20	−0.041	−0.146	pillow lavas
Sha8	22	0	−0.100	pillow lavas
Sha10	18	0	0	pillow lavas
Sha12	10	−0.301	−0.155	pillow lavas
Sha13	11	0	0	flaggy chalks, limestones
Sha14	12	0	0	flaggy chalks, limestones
Sha15	12	0	0	flaggy chalks, limestones
Sha16	10	0	0	red soil, chalk

[a]See *Danladi* [1997] for survey location.

Table A2. Variation of Overburden Resistivity and Static Shift Along a Regional Transect (A) With 10–20 km Station Spacing in the Eastern Part of Parnaiba Basin, Brazil[a]

Station	AOR, Ω m	S-TE	S-TM	Local Geology
A01	300	0	0	Precambrian migmatite
A02	20	−0.217	−0.218	SDsg
A03	330	−0.231	−0.176	SDsg
Ap3	160	0.301	0.097	Dp, basalt flow
Ap4	143	−0.162	−0.176	Dp
A04	102	0.097	−0.447	Dc
A05	33	−0.114	−0.0502	Dc
A06	50	−0.079	−0.415	Dc
A07	100	−0.079	−0.380	Dc
A08	33	−0.231	−0.079	Longa shale
A09	23	−0.079	0	Longa shale
A10	9	−0.041	0	sandstone
A11	7.8	−0.079	0	sandstone
A12	30	−0.174	0	sandstone
A13	40	0	0	sandstone
A14	8.5	0	−0.204	clay/siltstone
A15	9	−0.097	0.045	clay/siltstone
A16	20	−0.130	0.037	sandstone
A17	20	−0.301	−0.218	sandstone
A18	24	−0.231	−0.256	sandstone
A33	25	0	0	sandstone
A36	30	0	0	sandstone
A19	137	0	−0.322	sandstone
A20	30	−0.124	−0.218	clay/silt

[a]See *Meju et al.* [1999, Figure 2] for location. SDsg, Silurian-Devonian Serra Grande group of formations (continental sandstone); Dp, Devonian Pimenteiras shale; Dc, Devonian Cabecas (sandstone and siltstone) formation.

resistivities and static shifts significantly reduces structure solely due to static shifts and improves the overall resolution. It is also shown that the joint inversion approach works equally well in the presence of frequency-dependent shifts arising from elongate 3-D surficial bodies (that are long enough to allow some induction effect), irrespective

Table A3. Variation of Overburden Resistivity and Static Shift Along a Regional Transect (B) With 10 km Station Spacing in the Southern Part of Parnaiba Basin, Brazil[a]

Station	AOR, Ω m	S-TE	S-TM	Local Geology
B01	60	−0.362	−0.363	sandstone
B02	4800	−0.255	−0.362	dry sand
B03	2000	−0.267	−0.279	dry sand
B04	20	−0.021	0.097	siltstone/red soil
B05	35	−0.301	0.223	siltstone
B06	500	−0.362	−0.146	SDsg
B07	60	−0.347	−0.367	hard siltstone
B08	1550	−0.159	−0.356	basalt
B09	1000	−0.363	−0.432	hard sandstone
B10	95	0.721	0.522	Dp
B11	100	−0.454	−0.848	Dc
B12	106	−0.699	−0.477	Dc
B13	102	−0.504	−0.654	Dc
B14	108	−0.362	−0.903	Dc
B15	150	−1.40	−0.903	Dc
B16	280	0	0	massive sandstone
B17	500	0	0.0	massive sandstone
B18	216	0	0.223	SDsg
B19	280	0	−0.252	SDsg(cross-bedded)
B20	300	0.187	0.097	SDsg(+loamy soil)
B21	24	−0.115	−0.114	sandstone

[a]See *Meju et al.* [1999, Figure 2] for location. SDsg, Silurian-Devonian Serra Grande group of formations (continental sandstone); Dp, Devonian Pimenteiras shale; Dc, Devonian Cabecas (sandstone and siltstone) formation.

Table A4. Variation of Overburden Resistivity and Static Shift Along a Regional Transect With 10–20 km Station Spacing in Southern Kenya[a]

Station	AOR, Ω m	S-TE	S-TM	Local Geology
Nyamanga	13.2	−0.602	0.638	Mv (nephelinites)
Migori	405	−0.380	−0.204	rhyolites
Kihancha	330	0	0	rhyolites
Lolkoroin	70	0.854	0.699	metabasalts, pillow lavas
Oloololo	14	−0.190	0.155	phonolite, trachytes, basalts
Keekorok	551	0	0	P0 (crystalline basement)
Leganishu	90	−0.301	−0.079	P0 (crystalline basement)
Morijo	295	−0.699	−0.602	P0 + alluvium
Irkimba	20	−0.146	−1.131	P0 + alluvium
Oloibortoto	12.5	−0.279	0	P0 (crystalline basement)
Magadi	50	0.187	0.824	trachyte and basalt lavas
Singleraine	18	0.301	0.155	trachyte and basalt lavas
Lukenya	63	0	−0.362	sediments over basement
Selengei	200	0	0	P0 + volcanics
Chyulu North	168	0.222	−0.424	Qv (volcanic belt)
Chyulu West	250	0.774	1.745	Qv (volcanic belt)
Chyulu Range	600	0.774	0.796	Qv (volcanic belt)
Chyulu South	40	−0.176	0.301	P0 (crystalline basement)
Mwatete	22	0	0.959	P0 (crystalline basement)

[a]See *Simpson et al.* [1997, Figure 1] for locations. Qv, Quaternary volcanics (basalt flows, pyroclastics, ash, and volcanic soils); Mv, Miocene volcanics; P0, Precambrian rocks (granulites, amphibolites, migmatites, granites, and gneiss).

of whether it employs zero sum or Gaussian constraint on the distribution of static shifts.

Appendix A: Variation of Overburden Resistivity and Static Shift With Lithology at Different Spatial Scales

[21] Tables A1–A4 give the summaries of the anomalous overburden resistivity (AOR) determined by the inversion of central loop TEM soundings, static shift parameters in the log domain (S) determined for the dual-polarization MT apparent resistivity curves using collocated multigeometry (central, single, and offset loop) TEM soundings, and the local geological features for different geological terrains.

References

Berdichevsky, M. N., and V. I. Dmitriev (1976), Distortion of magnetic and electric fields by near-surface lateral inhomogeneities, *Acta Geodaet. Geophys. Mantanist. Acad. Sci. Hung.*, 11, 447–484.

Danladi, R. (1997), Integrated magnetotelluric and transient electromagnetic studies of structural control on massive sulphide mineralisation in part of northeastern Troodos ophiolite complex, Cyprus, Ph.D. thesis, 172 pp, Univ. of Leicester, Leicester, U.K.

deGroot-Hedlin, C. (1991), Removal of static shift in two dimensions by regularized inversion, *Geophysics*, 56, 2102–2106.

Groom, R. W., and R. C. Bailey (1989), Decomposition of magnetotelluric impedance tensors in the presence of local three-dimensional galvanic distortion, *J. Geophys. Res.*, 94, 1913–1925.

Jones, A. G. (1988), Static shift of magnetotelluric data and its removal in a sedimentary basin environment, *Geophysics*, 53, 967–978.

Mackie, R. L., and T. R. Madden (1993), Three-dimensional magnetotelluric inversion using conjugate gradients, *Geophys. J. Int.*, 115, 215–229.

Meju, M. A. (1996), Joint inversion of TEM and distorted MT soundings: Some effective practical considerations, *Geophysics*, 61, 56–65.

Meju, M. A. (2002), Geoelectromagnetic exploration for natural resources: Models, case studies and challenges, *Surv. Geophys.*, 23, 133–205.

Meju, M. A. (2005), Simple relative space-time scaling of electrical and electromagnetic depth sounding arrays: Implications for static shift

removal and joint DC-TEM data inversion with the most-squares criterion, *Geophys. Prospect.*, *53*, 463–479.

Meju, M. A., S. L. Fontes, M. F. B. Oliveira, J. P. R. Lima, E. U. Ulugergerli, and A. A. Carrasquilla (1999), Regional aquifer mapping using combined VES-TEM-AMT/EMAP methods in the semi-arid eastern margin of Parnaiba Basin, Brazil, *Geophysics*, *64*, 337–356.

Meju, M. A., S. L. Fontes, E. U. Ulugergerli, E. F. La Terra, C. R. Germano, and R. M. Carvalho (2001), A joint TEM-HLEM geophysical approach to borehole siting in deeply-weathered granitic terrains, *Ground Water*, *39*, 554–567.

Mohamed, A. K., M. A. Meju, and S. L. Fontes (2002), Deep structure of the northeastern margin of Parnaiba basin, Brazil, from magnetotelluric imaging, *Geophys. Prospect.*, *50*, 589–602.

Newman, G. A., and D. L. Alumbaugh (2000), Three-dimensional magnetotelluric inversion using non-linear conjugate gradients, *Geophys. J. Int.*, *140*, 410–424.

Ogawa, Y., and T. Uchida (1996), A two-dimensional magnetotelluric inversion assuming Gaussian static shift, *Geophys. J. Int.*, *126*, 69–76.

Palacky, G. J. (1987), Resistivity characteristics of geological targets, in *Electromagnetic Methods in Applied Geophysics–Theory*, vol. 1, *Invest. Geophys. Ser.*, vol. 3, edited by M. N. Nabighian, pp. 53–129, Soc. of Exp. Geophys., Tulsa, Okla.

Pellerin, L., and G. W. Hohmann (1990), Transient electromagnetic inversion: A remedy for magnetotelluric static shifts, *Geophysics*, *55*, 1242–1250.

Sakkas, V., M. A. Meju, M. A. Khan, V. Haak, and F. Simpson (2002), Magnetotelluric images of the crustal structure of Chyulu Hills volcanic field, Kenya, *Tectonophysics*, *346*, 169–185.

Sasaki, Y. (2004), Three-dimensional inversion of static-shifted magnetotelluric data, *Earth Planets Space*, *56*, 239–248.

Simpson, F. L., V. Haak, M. A. Khan, V. Sakkas, and M. A. Meju (1997), The KRISP-94 magnetotelluric survey of early 1995: First results, *Tectonophysics*, *278*, 261–272.

Siripunvaraporn, W., G. Egbert, Y. Lenbury, and M. Uyeshima (2005), Three-dimensional magnetotelluric inversion: Data-space method, *Phys. Earth Planet. Inter.*, *150*, 3–14.

Smith, J. T. (1996), Conservative modeling of 3-D electromagnetic fields: part II, Biconjugate gradient solution and an accelerator, *Geophysics*, *61*, 1319–1324.

Sternberg, B. K., J. C. Washburne, and L. Pellerin (1988), Correction for the static shift in magnetotellurics using transient electromagnetic soundings, *Geophysics*, *53*, 1459–1468.

Torres-Verdin, C., and F. X. Bostick (1992), Principles of spatial surface electric fields filtering in magnetotellurics: Electromagnetic array profiling (EMAP), *Geophysics*, *57*, 603–622.

Wannamaker, P. E., G. W. Hohmann, and S. H. Ward (1984), Magnetotelluric responses of three-dimensional bodies in layered earths, *Geophysics*, *49*, 1517–1533.

―――――――――――――

M. A. Meju, Department of Environmental Science, Lancaster University, Lancaster LA14YQ, UK. (m.meju@lancaster.ac.uk)

Y. Sasaki, Department of Earth Resources Engineering, Kyushu University, Fukuoka 812-8581, Japan. (sasaki@mine.kyushu-u.ac.jp)